

Examining the Role of Surfactant Packing in Phase Transformations of Periodic Templated Silica/Surfactant Composites

Amelia M. Lapeña, Adam F. Gross, and Sarah H. Tolbert*

Department of Chemistry and Biochemistry, University of California,
Los Angeles, California 90095-1569

Received June 16, 2004. In Final Form: September 30, 2004

In this work, we examine the role of curvature and surfactant packing in controlling the structure of periodic silica/surfactant composites by driving such materials through a transformation from a hexagonal to a lamellar phase. We focus on how the interplay of desired packing and volume constraints dictates the resulting structures. In general, surfactants expand in a complex way upon heating, and this can cause a change in the optimal packing geometry. However, the presence of a rigid silica framework may prevent surfactants from reaching this preferred volume and/or curvature. Real-time in situ X-ray diffraction is used to monitor the structural evolution of these materials heated under hydrothermal treatments. Because the thermal-driven disorder of the surfactant tails drives the phase transition, we examine four types of composites with varying tail density. Ordinarily, composites consist of surfactants with one 20-carbon tail and one positively charged ammonium headgroup. Tail density is varied by replacing a small amount (0–16%) of these single-tail, single-head surfactants with single-tail, double-head ‘gemini’ surfactants. A greater head–tail ratio indeed produces different results, causing the phase transition to occur at higher temperatures. Using simple geometric models to gain better understanding of our experimental results, we find that, while both unfavorable curvature and limited volume may exist for the surfactants in these composites, the constrained curvature appears to be the dominant effect in driving structural rearrangement.

Introduction

Periodic hexagonal silica/surfactant nanostructures are interesting materials systems; they combine liquid-crystal packing with a rigid framework.^{1,2} Surfactants self-assemble to form liquid-crystal phases with long-range order, including a H_a -like phase consisting of hexagonally packed cylindrical micelles. Silica oligomers that associate with surfactant headgroups can then polymerize and form a highly ordered rigid framework. Although the cross-linked inorganic phase provides a major portion of the free energy change associated with composite formation,³ surfactant curvature plays a significant role in the resulting liquid-crystal phase and has been exploited to synthesize additional structures using a range of different surfactants^{4–14} and organic additives (as cosurfactants).^{4,5,13–18} Curvature continues to be crucial in deter-

mining the final structure when the composite is treated to exhibit a phase transformation.^{4,13,19–25} Unfortunately, the function of curvature in mesostructural rearrangements is not well understood. It is well-known, however, that the curvature of a liquid-crystal phase is strongly related to how surfactants order.²⁶ In this work, we examine the role played by surfactant packing as our composites undergo mesostructural changes. Our experiments and models may provide a greater understanding on controlling composite structure, which could in turn allow for more rational design of materials for size-selective applications such as chromatography.^{27–34}

- (1) Kresge, C. T.; Leonowicz, M. E.; Roth, W. J.; Vartuli, J. C.; Beck, J. S. *Nature* **1992**, *359*, 710.
- (2) Beck, J. S.; Vartuli, J. C.; Roth, W. J.; Leonowicz, M. E.; Kresge, C. T.; Schmitt, K. D.; Chu, C. T.-W.; Olson, D. H.; Sheppard, E. W.; McCullen, S. B.; Higgins, J. B.; Schlenker, J. L. *J. Am. Chem. Soc.* **1992**, *114*, 10834.
- (3) Huo, Q. S.; Margolese, D. I.; Ciesla, U.; Demuth, D. G.; Feng, P. Y.; Gier, T. E.; Sieger, P.; Firouzi, A.; Chmelka, B. F.; Schüth, F.; Stucky, G. D. *Chem. Mater.* **1994**, *6*, 1176.
- (4) Huo, Q. S.; Margolese, D. I.; Stucky, G. D. *Chem. Mater.* **1996**, *8*, 1147.
- (5) Raman, N. K.; Anderson, M. T.; Brinker, C. J. *Chem. Mater.* **1996**, *8*, 1682.
- (6) Chen, F.; Huang, L.; Li, Q. *Chem. Mater.* **1997**, *9*, 2685.
- (7) Ryoo, R.; Ko, C. H.; Park, I.-S. *Chem. Commun.* **1999**, *15*, 1413.
- (8) Ryoo, R.; Joo, S. H.; Kim, J. M. *J. Phys. Chem. B.* **1999**, *103*, 7435.
- (9) Coleman, N. R. B.; Attard, G. S. *Micropor. Mesopor. Mater.* **2001**, *44–45*, 73.
- (10) Dai, L.-R.; Wang, T.-W.; Bu, L.-T.; Chen, G. *Colloids Surf., A* **2001**, *181*, 151.
- (11) Kapoor, M. P.; Inagaki, S. *Chem. Mater.* **2002**, *14*, 3509.
- (12) Shen, S. D.; Li, Y. Q.; Zhang, Z. D.; Fan, J.; Tu, B.; Zhou, W. Z.; Zhao, D. Y. *Chem. Commun.* **2002**, 2212.
- (13) Lin, H. P.; Mou, C. Y. *Acc. Chem. Res.* **2002**, *35*, 927.
- (14) Lind, A.; Spliethoff, B.; Lindén, M. *Chem. Mater.* **2003**, *15*, 813.

- (15) Ågren, P.; Lindén, M.; Rosenholm, J. B.; Schwarzenbacher, R.; Krichbaum, M.; Amenitsch, H.; Laggner, P.; Blanchard, J.; Schüth, F. *J. Phys. Chem. B.* **1999**, *103*, 5493.
- (16) Tiemann, M.; Goletto, V.; Blum, R.; Babonneau, F.; Amenitsch, H.; Lindén, M. *Langmuir* **2002**, *18*, 10053.
- (17) Kleitz, F.; Blanchard, J.; Zibrowius, B.; Schüth, F.; Ågren, P.; Lindén, M. *Langmuir* **2002**, *18*, 4963.
- (18) Liu, S. Q.; Cool, P.; Collart, O.; Van Der Voort, P.; Vansant, E. F.; Lebedev, O. I.; Van Tendeloo, G.; Jiang, M. H. *J. Phys. Chem. B* **2003**, *107*, 10405.
- (19) Gallis, K. W.; Landry, C. C. *Chem. Mater.* **1997**, *9*, 2035.
- (20) Pevzner, S.; Regev, O. *Micropor. Mesopor. Mater.* **2000**, *38*, 413.
- (21) Landry, C. C.; Tolbert, S. H.; Gallis, K. W.; Monnier, A.; Stucky, G. D.; Norby, P.; Hanson, J. C. *Chem. Mater.* **2001**, *13*, 1600.
- (22) Tolbert, S. H.; Landry, C. C.; Stucky, G. D.; Chmelka, B. F.; Norby, P.; Hanson, J. C.; Monnier, A. *Chem. Mater.* **2001**, *13*, 2247.
- (23) Gross, A. F.; Le, V. H.; Kirsch, B. L.; Tolbert, S. H. *Langmuir* **2001**, *17*, 3496.
- (24) Che, S.; Kamiya, S.; Terasaki, O.; Tatsumi, T. *J. Am. Chem. Soc.* **2001**, *123*, 12089.
- (25) Carreon, M. A.; Gulians, V. V. *Catal. Today* **2003**, *78*, 303. This work was done on vanadium–phosphorus oxides, but phase transformations reveal a strong relation between surfactant packing and final mesostructures.
- (26) Israelachvili, J. *Intermolecular & Surface Forces*, 2nd ed; Academic Press: California, 1992.
- (27) Grün, M.; Kurganov, A. A.; Schacht, S.; Schüth, F.; Unger, K. K. *J. Chromatogr. A* **1996**, *740*, 1.
- (28) Feng, X.; Fryxell, G. E.; Wang, L.-Q.; Kim, A. Y.; Liu, J.; Kenner, K. M. *Science* **1997**, *276*, 923.

To understand how packing affects phase stability, composites are heated and forced to undergo a hexagonal-to-lamellar phase transition. Heating induces conformational disorder of surfactant tails. The increased tail motion changes the effective volume and shape occupied by a surfactant. The volume and shape, in turn, determine the surfactant's desired packing and curvature. The silica framework, however, limits the available space, and thus, surfactants are unable to occupy their preferred volume and/or attain their preferred curvature; the surfactant volume and/or curvature become frustrated. Eventually this packing frustration overcomes the strength of the covalent bonds in the silica network, and the hexagonally packed silica cylinders transform to silica bilayers (i.e., the lamellar phase). We examine how these volume and curvature effects alter surfactant packing and drive structural rearrangements.

To study curvature effects, we monitor the evolution of the surfactant packing shape as the composites are heated. Israelachvili²⁶ quantitatively assigned the packing shape of a surfactant through a geometric packing parameter, g , which is defined as the ratio of the surfactant volume to the product of the head-surface interfacial area and the surfactant length. With a known g value, we can determine the surfactant curvature and the phase of the resulting mesostructure.²⁶ For example, single-head, single-tail surfactants with short hydrophobic tails and large hydrophilic heads tend to pack as spheres. Most of the tails aggregate inside the sphere to minimize their contact with water. This situation gives rise to a small g value; the packing shape is a cone and the preferred curvature is high. Low-curvature structures, such as flat bilayers, possess larger g values and can arise from double-tail surfactants with a cylindrical packing shape. The packing parameter also depends on laboratory conditions. For example, surfactants with a larger thermal expansion coefficient for tails than for heads may pack as truncated cones (e.g., large head volume, small tail volume) at room temperature but then pack as cylinders (e.g., large head volume, large tail volume) at much higher temperatures.

In this paper, we study how surfactant packing determines the structure of silica/surfactant composites. Because the thermally induced motion of the surfactant tails provides the main drive for structural change, varying tail concentration may provide insight into the composite's phase behavior. Specifically, we replace a small percentage of the single-tail, single-head surfactants with single-tail, double-head gemini surfactants and synthesize composites with similar pore sizes but differing head:tail ratios. Phase transitions are tracked using in situ low-angle X-ray diffraction (XRD). We apply simple geometric models and Israelachvili's packing parameter, g , to understand the XRD data and to examine how surfactant packing dictates the resulting silica/surfactant mesostructure through the interplay of volume and curvature.

Experimental Section

Two types of surfactants were used to template the silica mesostructures: a 'regular' surfactant, $\text{CH}_3(\text{CH}_2)_{19}\text{N}(\text{CH}_3)_3\text{Br}$,

and a 'gemini' surfactant, $[\text{CH}_3(\text{CH}_2)_{19}\text{N}(\text{CH}_3)_2](\text{CH}_2)_3[\text{N}(\text{CH}_3)_3]\text{Br}_2$. Although both surfactants possess one 20-carbon (hydrophobic) tail, the regular surfactant has only one quaternary ammonium head, while the gemini surfactant has two heads that are linked by a short three-carbon spacer. The regular surfactant was synthesized from $\text{N}(\text{CH}_3)_3\text{Br}$ and $\text{CH}_3(\text{CH}_2)_{19}\text{Br}$ using known methods.³⁵ The gemini surfactant was synthesized in a similar fashion. Initially, the 20-carbon tail was added to an amine head by mixing 9.0 g of $\text{CH}_3(\text{CH}_2)_{19}\text{Br}$ and 100 mL of $\text{HN}(\text{CH}_3)_2$ in 100 g of pure ethanol. This mixture was stirred under argon at about 40 °C for 6 days. The product was filtered, recrystallized twice, and air-dried at room temperature. This ammonium surfactant was then dissolved in excess base (NaOH) to produce the amine $\text{CH}_3(\text{CH}_2)_{19}\text{N}(\text{CH}_3)_2$. Finally, the linker and second headgroup were added by mixing the amine surfactant with $\text{Br}(\text{CH}_2)_3\text{N}(\text{CH}_3)_3\text{Br}$ such that the amine surfactant was 5% in excess. This mixture was dissolved in 100 g of pure ethanol and stirred under argon at 90 °C for 2 days. The final product was filtered, recrystallized, and air-dried at room temperature. ¹H NMR using a Bruker AC200 spectrometer was used to confirm both surfactant structures.

Four types of silica/surfactant composites were made by varying the amount of gemini surfactants while keeping total surfactant amount constant. Synthesis compositions of gemini were 0%, 10%, 20%, and 30% (based on constant total moles of heads) for the four different composites. Actual gemini fractions were determined through elemental analysis (Desert Analytics, Tucson, AZ) from C:N ratios. In the composite synthesis, 2.73 mmol of surfactants was dissolved in 11.548 g of a 0.218 M NaOH solution. The mixture was heated slightly to aid surfactant dissolution. Once the solution cooled to 45 °C, 0.965 g of tetraethyl orthosilicate (TEOS) was added and the mixture was stirred for 1 h. The resulting composites were filtered, washed with water, and air-dried at room temperature.

Phase behavior for each sample was monitored using real-time low-angle X-ray powder diffraction (XRD) under hydrothermal conditions. General setup and data collection details can be found elsewhere.³⁵ Data were collected at the Stanford Synchrotron Radiation Laboratory on wiggler beamline 10-2 using an X-ray energy of 9 keV. For in situ heating, the temperature was increased at 4 °C/min and data were collected in 30 s acquisitions using a Roper Scientific 1242 × 1152 cooled X-ray CCD detector. Samples consisted of a 1:2 mixture (by weight) of composite/water. Three runs on each sample were conducted for statistics. Data were analyzed by fitting diffraction peaks with a Voigt function to determine peak areas and positions. The sample temperature was calibrated against the known melting points of sulfur and ascorbic acid.

Nitrogen adsorption/desorption data were collected on calcined mesopores to determine pore-size uniformity and surface area using a Micrometrics ASAP 2000 porosimeter. To produce porous silica samples, silica/surfactant composites were placed under flowing N_2 gas. The temperature was ramped from 25 to 500 °C at 1 °C/min and then held at 500 °C for 6 h. The gas was then changed to O_2 . Samples were kept at 500 °C for an additional 6 h and then cooled to room temperature at 2 °C/min. The degree of polymerization of the silica framework was measured using ²⁹Si solid-state magic angle spinning (MAS) NMR using a Bruker Avance 300 spectrometer with a standard one-pulse acquisition and a 240 s recycle delay.^{35,36}

Spartan molecular modeling software³⁷ allowed for simple molecular modeling of the surfactants. Molecular models were constructed to estimate physical quantities such as the volume and dimensions of the head. Spartan minimizes torsional angle and van der Waals strain to determine a relaxed geometry that corresponds to the local energy minimum closest to an initial configuration.

(35) Gross, A. F.; Ruiz, E. J.; Tolbert, S. H. *J. Phys. Chem. B* **2000**, 104, 5448.

(36) Gross, A. F.; Ruiz, E. J.; Le, V. H.; Tolbert, S. H. *Micropor. Mesopor. Mater.* **2001**, 44–45, 785.

(37) Spartan SGI Version 5.0.3 OpenGL (built under IRIX 6.2); Wavefunction, Inc.: Irvine, CA, 1991–1997.

(29) Raimondo, M.; Perez, G.; Sinibaldi, M.; De Stefanis, A.; Tomlinson, A. A. *G. Chem. Commun.* **1997**, 1343.

(30) Liu, J.; Feng, X.; Fryxell, G. E.; Wang, L.-Q.; Kim, A. Y.; Gong, M. *Adv. Mater.* **1998**, 10, 161.

(31) Gallis, K. W.; Araujo, J. T.; Duff, K. J.; Moore, J. G.; Landry, C. C. *Adv. Mater.* **1999**, 11, 1452.

(32) Nassivera, T.; Eklund, A. G.; Landry, C. C. *J. Chromatogr. A* **2002**, 973, 97.

(33) Ma, Y.; Qi, L.; Ma, J.; Wu, Y.; Liu, O.; Cheng, H. *Colloids Surf., A* **2003**, 229, 1.

(34) Shindo, T.; Kudo, H.; Kitabayashi, S.; Ozawa, S. *Micropor. Mesopor. Mater.* **2003**, 63, 97.

Table 1. Elemental and Surfactant Composition of the Various Composites

% gemini synthesis	% C	% H	% N	% Si	% other	% gemini actual ^a
0	42.11	8.44	2.20	16.90	30.36	0.0
10	40.97	8.26	2.23	17.87	30.68	9.5
20	40.12	8.18	2.24	20.57	28.91	12.9
30	39.96	8.02	2.28	19.69	30.07	16.2

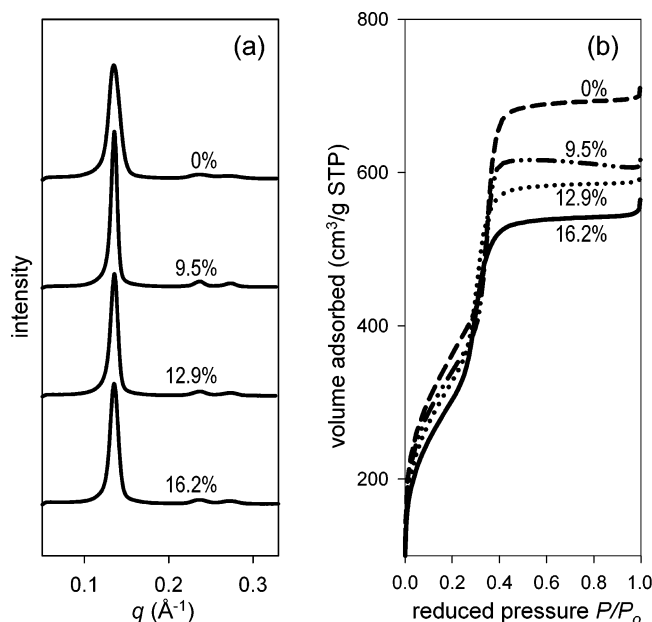
^a % Gemini = 100 x_{gemini} .

Figure 1. As-synthesized samples of varying gemini concentration are characterized for order and uniformity. Integrated XRD patterns (a) confirm initial samples possess hexagonal order with essentially identical peak positions. Curves are offset for clarity. N_2 adsorption curves (b) reveal pore sizes are nearly uniform. These results indicate silica/surfactant composites maintain good hexagonal order with a constant pore size when a small concentration of regular surfactants is replaced with gemini surfactants.

Results

A. Sample Characterization. 1. Elemental Analysis.

Mass percentages of carbon, hydrogen, nitrogen, and silicon for each composite are listed in Table 1. These composites should contain only silica and surfactants; the remaining element therefore must be oxygen. Furthermore, because we assume that the organic part consisted of surfactants only, the actual fraction (x_{gemini}) of gemini surfactants present in a given composite can be determined from the C:N ratios (Table 1). We note that hydrolysis of TEOS, which is the silica source for these composites, releases ethanol, which can remain inside the pores and provide excess carbon.³⁵ In these studies, however, no excess carbon was found for the composite containing no gemini surfactants (C:N = 23:1) and so all carbon was assumed to originate only from surfactants (regular and gemini) for all samples studied.

2. X-Ray Diffraction. Figure 1a shows integrated diffraction patterns of the initial hexagonal structures for the four samples. All composites display sharp, narrow peaks with good intensity, revealing well-ordered hexagonal frameworks. The largest peak, which represents the (10) fundamental peak, is situated at about $q = 0.14 \text{ \AA}^{-1}$ for all four samples; the presence of gemini surfactants has not only preserved the honeycomb silica framework but also maintained the same lattice constant, a_0 . The

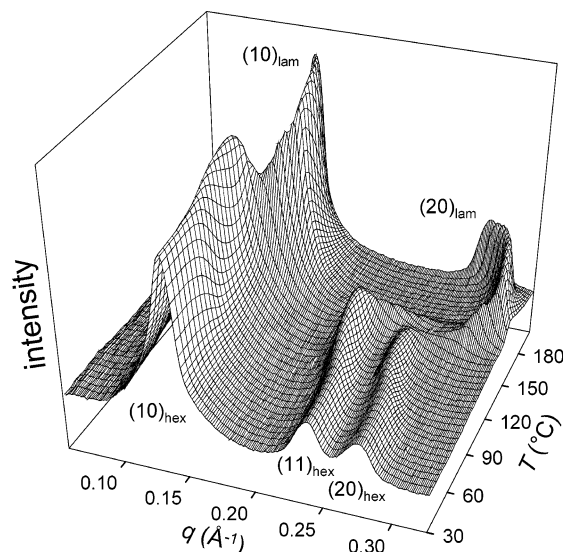


Figure 2. Real-time in situ low-angle XRD is used to track the phase behavior of hydrothermally treated silica/surfactant composites. Here, integrated XRD patterns illustrate the mesostructural evolution of a 9.5% gemini composite transforming from a hexagonal honeycomb phase (three peaks) to a lamellar phase (two peaks).

(11) and (20) higher-order peaks are located approximately at $q = 0.24 \text{ \AA}^{-1}$ and $q = 0.27 \text{ \AA}^{-1}$, respectively.

3. Nitrogen Adsorption / Desorption. Figure 1b illustrates typical nitrogen-adsorption behavior in these mesopores. We provide only adsorption data for plot simplicity; desorption curves are almost identical, revealing very little hystereses. Different plots represent different samples. The steep change found in each curve indicates a narrow pore-size distribution within each composite. Similar values of the reduced pressure at which capillary condensation occurs reveal similar initial pore sizes among the different composites.

B. In Situ X-Ray Scattering. Real-time XRD was used to monitor composite structure and order as samples were heated with a linear heating ramp. Figure 2 shows such data for a 9.5% gemini sample. The graph depicts the general mesostructural evolution from a hexagonal honeycomb phase to a lamellar phase. As the sample is heated, the (10)_{hex}, (11)_{hex}, and (20)_{hex} hexagonal peaks initially grow in intensity and narrow in width. At higher temperatures, these peaks lose intensity and move slightly toward a greater q . The appearance of equally spaced (10)_{lam} and (20)_{lam} peaks at higher temperatures indicates that a lamellar phase has formed. Broad peaks with lower intensities are actually the overlap of hexagonal and lamellar peaks. These are found in the intermediate temperatures, representing the coexistence of the hexagonal and lamellar phases. The broadening and drop in intensity of the hexagonal peaks occurs as the hexagonally packed silica cylinders restructure to form bilayers of silica and surfactants. With further heating, the hexagonal peaks disappear, while the lamellar peaks narrow in width and grow in intensity.

Figure 2 also shows that the hexagonal and lamellar phases coexist in a wide temperature range. However, the transition temperature, $T_{\text{transition}}$, is specified as an approximate midpoint temperature at which equal amounts of both phases exist. As illustrated in Figure 3a for the 9.5% gemini sample, the integrated area of the fundamental (10)_{hex} peak is plotted as a function of temperature and the temperature where this peak area has decreased to 50% of its maximum area is $T_{\text{transition}}$.

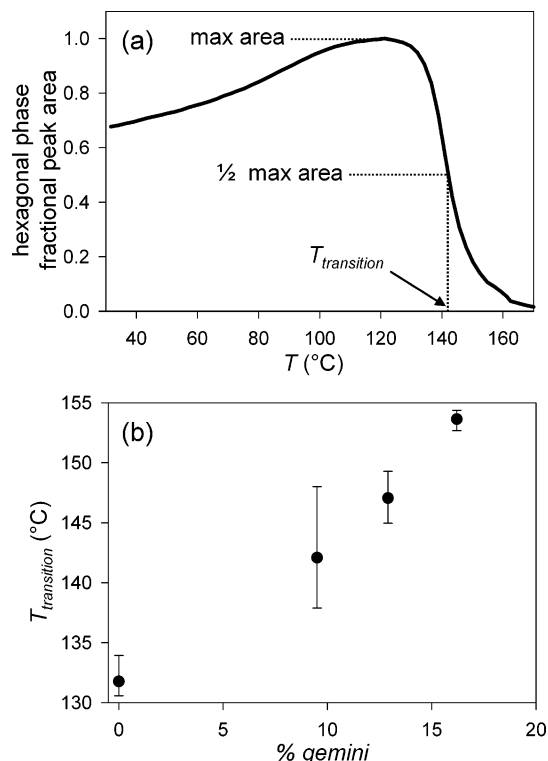


Figure 3. Defined as the temperature at which half the hexagonal phase has transformed, $T_{\text{transition}}$ is assigned to the point where the fundamental peak area of the hexagonal phase has decreased by half, as illustrated in (a) for a 9.5% gemini sample. Increasing the gemini concentration leads to higher $T_{\text{transition}}$ values, as shown in (b). More thermal energy is needed to transform a composite with a lower density of surfactant tails.

Plotted for the different composites in Figure 3b, each $T_{\text{transition}}$ is the average value based on three experimental heating runs. We find that a direct relationship between $T_{\text{transition}}$ and % gemini exists. An increase in % gemini is equivalent to a decrease in the surfactant tail concentration present in the pores. Because the thermally disordered tails propel structural rearrangements, more energy and thus a greater temperature are needed with fewer tails to drive the hexagonal–lamellar phase transition. The Discussion section explores how this thermally induced tail motion produces this $T_{\text{transition}}$ trend.

Another way to examine a composite's phase behavior is to track the fundamental hexagonal peak position from XRD data. Values for the lattice constant, a_o , are calculated using the known relation for a hexagonal unit cell, $a_o = 2/\sqrt{3} (d_{10})$. Plots of $a_o(T)$ for our four samples are given in Figure 4. General trends are as follows: At room and slightly above temperatures, there are no significant structural changes and a_o changes only slightly. The silica walls are undergoing further polymerization, however.^{35,36} At higher temperatures, a_o increases dramatically; molecular thermal expansion of the organic phase swells the unit cell. Eventually a_o reaches a maximum and then begins to decrease at the onset of the phase transition. We note that we only use a_o values up to the point where approximately 10% of the composite has transformed. After this point, overlapping peaks make the fits untrustworthy.

Discussion

Hydrothermally treated silica/surfactant composites can undergo structural changes. While surfactants tend to expand upon heating, the cross-linked silica restricts the

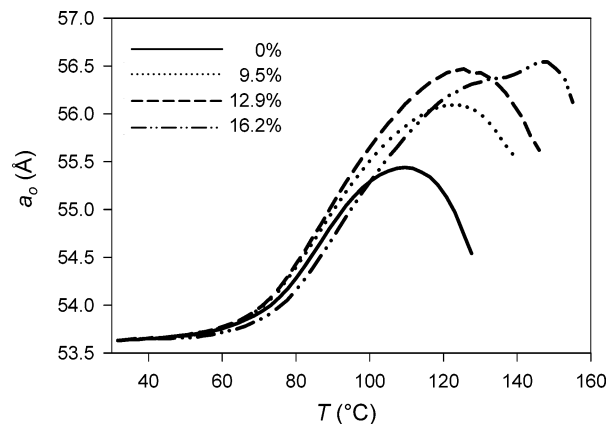


Figure 4. The hexagonal lattice constant, a_o , is a useful geometric parameter to track the behavior of a composite undergoing structural changes when heated in water. Values for a_o are determined from the fundamental peak position of the hexagonal phase. Changes in a_o are illustrated here for various % gemini samples. Generally, increasing gemini concentration results in greater total pore expansion and higher hexagonal–lamellar transition temperatures.

available volume and limits surfactant expansion. With sufficient heating, however, silica bond breaking occurs and allows for a phase transition. Here we examine how the surfactants control this phase behavior, assuming two possible ways: (1) the thermal disorder of the tails provides a simple expansive pressure; (2) the increased motion of the tails changes the preferred surfactant curvature. The true role played by surfactant packing most likely exists as an interplay of both volume and curvature effects, but one may dominate. In the discussion to follow, we model limiting cases to examine how changes in surfactant packing may drive structural rearrangement when surfactants are surrounded by a highly interconnected inorganic phase.

Our general goal is to determine how heating surfactants in the presence of the cross-linked silica changes the average surfactant volume and curvature. To do this, we take structural parameters from our XRD data on the four composites with varying gemini surfactant concentration. We then apply temperature-dependent geometric models to see how surfactant packing evolves as composites undergo hydrothermal treatment. These results are compared with those calculated for the same surfactant with no rigid silica barrier to prevent optimal volume and/or shape changes.

A. Modeling the Starting Configuration. Sample characterization is used to establish that our composites begin in a hexagonal honeycomb phase with a narrow pore-size distribution, allowing us to model these materials as highly ordered, hexagonally packed cylinders of equal radii. (See Figure 5a.) In our modeling, we assume homogeneous mixing between gemini and regular (single-head) surfactants. In the event of partial phase separation, it could be possible for the gemini surfactant (which tend to form sphere-based phases) to drive the formation of an undulating hexagonal phase with corrugated pores. Because the quality and shape of the diffraction patterns are basically identical for 0% gemini and 16% gemini materials, however, we feel that such phase separation is unlikely and thus our assumption of cylindrical pores is valid.

Volume and curvature changes are monitored through the evolution of the pore radius, r_p , as samples are heated in water. Radii values are taken from XRD data, which provide the lattice constant, a_o , as a function of temper-

Table 2. Measured and Calculated Geometric Parameters for Calcined Samples

% gemini	A_s (m ² /g)	V_p (cm ³ /g)	r_p (Å)	a_o (Å)	A_w (Å ² /unit cell)	$V_w = A_w h$ (cm ³ /g)	t_w (Å)
0.0	1043	0.8533	16.4	43.3	2352	2.39	10.6
9.5	1129	0.9107	16.1	43.1	2370	2.64	10.8
12.9	1251	1.0807	17.3	45.7	2602	3.00	11.1
16.2	1177	0.9408	16.0	45.3	2929	3.43	13.4

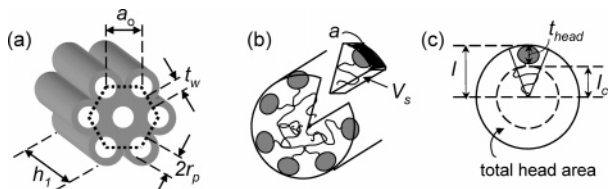


Figure 5. Simple geometric models allow for structural examination of surfactant-templated silica. As shown in (a), composites are hexagonally packed cylinders with uniform pore size. The gray region denotes the silica framework; white regions represent organic domains when uncalcined and empty pores when calcined. The lattice constant, a_o , consists of the wall thickness, t_w , and the pore radius, r_p . The cylindrical length of the long axis is h_1 ; the total for all cylinders is h . Illustrations (b) and (c) show that a pie wedge can be used to describe the surfactant packing shape. V_s is the surfactant volume and a is the head-silica interfacial area. The surfactant length, l , is a sum of the effective tail length, l_c , and the head thickness, t_{head} .

ature, T . Values for a_o also contain the silica wall thickness, t_w , and are given by eq 1. For moderate heating temperatures, we assume that t_w remains constant with heating for all samples synthesized under the same conditions.

$$a_o(T) = 2r_p(T) + t_w \quad (1)$$

Measuring t_w for our composite materials, however, is not a simple matter. Experiments to determine pore size and wall thickness are usually done on materials in which the organic phase has been removed by calcination.^{38,39} Using a combination of N₂ adsorption/desorption data and low-angle XRD, we can easily measure t_w for calcined samples since the pores remain intact due to strong cross-linking among silica molecules. However, calcination also promotes further framework polymerization and thus alters the samples. Water is expelled, walls become denser, and the pore-to-pore repeat distance shrinks. We thus use the approximation that the fractional wall mass decrease and the fractional wall density increase are equal to allow us to calculate the wall density for the *uncalcined* composite. From this, we can determine other parameters for the uncalcined sample, particularly t_w .

$$\frac{V_p}{A_s} = \frac{1}{2}r_p(T_{initial}) = \frac{1}{4}[a_o(T_{initial}) - t_w] \quad (2)$$

To measure t_w for *calcined* samples, we combine eq 1 with geometric formulas for a right cylinder and establish the expressions in eq 2. The pore volume, V_p , and the pore surface area, A_s , are known from N₂ adsorption/desorption data. In addition, other geometric relations, such as the hexagonal unit cell, are used to compute the cross-sectional wall area per hexagonal unit cell, A_w , and the total wall volume, V_w . All values for calcined samples that were synthesized with varying gemini concentration are shown in Table 2. Values for total cylindrical lengths h (Å/g) are chosen such that correct A_s and V_p values were recovered.

Table 3. Geometric Parameters for Uncalcined Samples

% gemini	a_o (Å)	V_w (cm ³ /g)	A_w (Å ² /unit cell)	r_p (Å)	t_w (Å)
0.0	52.9	2.51	2435	22.7	7.60
9.5	52.9	2.78	2454	22.6	7.69
12.9	52.8	3.16	2694	22.0	8.85
16.2	53.8	3.62	3033	21.8	10.2

The t_w values listed in Table 2 are then scaled for calcination shrinkage to estimate t_w for *uncalcined* composites. We estimate the scaling factor by using ²⁹Si solid-state MAS NMR spectroscopy^{35,36} to measure the additional silica polymerization caused by calcination. The degree of polymerization for both *uncalcined* and *calcined* samples are determined from Q^4 and Q^3 peak areas, where Q^4 is defined as $\text{Si}-(\text{OSi})_4 = \text{SiO}_2$ and Q^3 is defined as $(\text{SiO})_3-\text{Si}-\text{OH}$ or $(\text{SiO})_3-\text{Si}-\text{O}^- = \text{SiO}_{2.5}$. The ratio of Q^4/Q^3 peak areas corresponds to a molar ratio between SiO_2 and $\text{SiO}_{2.5}$. Therefore, a Q^4/Q^3 value of 1.96 gives a wall stoichiometry of $\text{SiO}_{2.17}$ for the calcined sample, while a Q^4/Q^3 of 0.84 yields $\text{SiO}_{2.27}$ for the uncalcined sample.^{40,41} With these stoichiometries, we calculate the fractional wall mass decrease. Because we set this fractional wall mass decrease equal to the fractional wall density increase, we can scale the measured calcined wall density⁴⁰ of 2.02 g/cm³ to get the wall density and the total wall volume, V_w , for an *uncalcined* composite. Furthermore, we can estimate the cross-sectional unit cell wall area, A_w , using eq 3 with values from Table 2. Equation 4 then applies the geometric formula for a hexagonal unit cell to determine the initial *uncalcined* pore radius. Finally, with eq 1 and a_o values in Table 3, we calculate wall thickness values (t_w) for the original uncalcined samples. Results are listed in Table 3.

$$A_w^{\text{uncalcined}} = A_w^{\text{calcined}} + \Delta A_w = A_w^{\text{calcined}} + \frac{2}{3} \frac{1}{h_{\text{calcined}}} (V_w^{\text{uncalcined}} - V_w^{\text{calcined}}) \quad (3)$$

$$r_p^{\text{uncalcined}}(T_{\text{initial}}) = \sqrt{\frac{\sqrt{3}}{2\pi} (a_o^{\text{uncalcined}}(T_{\text{initial}}))^2 - A_w^{\text{uncalcined}}} \quad (4)$$

Assuming t_w is the same for all composites synthesized under the same conditions with the same gemini concentration, we now can apply eq 1 to calculate the average pore radii, $r_p(T)$, for our *uncalcined* composites studied in situ. Initial values are listed in Table 4.

B. Changes in Volume and Curvature with Heating. To examine how the thermal disorder of the surfactant tails propels structural changes in the presence of a wall barrier, we use the T -dependent radii values, r_p , to calculate volume expansion, $V_s(T)$, and curvature evolution, $g(T)$, for an “average” surfactant. Most of our samples contain two types of surfactants, regular (single-head) and gemini. A *surfactant volume* or a *surfactant packing*

(38) Fenelonov, V. B.; Romannikov, V. N.; Derevyankin, A. Y. *Micropor. Mesopor. Mater.* **1999**, *28*, 57.

(39) Kruk, M.; Jaroniec, M.; Sakamoto, Y.; Terasaki, O.; Ryoo, R.; Ko, C. H. *J. Phys. Chem. B* **2000**, *104*, 292.

(40) Wu, J.; Liu, X.; Tolbert, S. H. *J. Phys. Chem. B* **2000**, *104*, 11837.

(41) We use one Q^4/Q^3 value for all calcined samples and one value for uncalcined samples. The uncalcined value is the Q^4/Q^3 value for the 0% gemini sample, determined by ²⁹Si MAS NMR. The calcined value is for a similar sample, taken from ref 40.

Table 4. Initial Lattice Constants (a_0), Wall Thicknesses (t_w), and Pore Radii (r_p) for Our Four Samples

% gemini	a_0 (Å)	t_w (Å)	r_p (Å)
0.0	53.6	7.60	23.0
9.5	53.6	7.69	23.0
12.9	53.6	8.85	22.4
16.2	53.6	10.2	21.7

shape, however, describes an *average* surfactant. This artificial surfactant is a weighted average of the regular and gemini surfactants, assuming that gemini surfactants are evenly distributed among regular surfactants. All calculations will deal with such *average* surfactants.

Volumes are straightforward calculations. As already shown in Figure 5a, surfactant aggregates occupy volume as right cylinders. Therefore, the total pore volume available to all surfactants evolves as a solid cylinder with $r_p(T)$ as input. We estimate the number of surfactants in a pore and, assuming no surfactant loss upon heating, determine the pore volume, $V_s(T)$, available to a surfactant.

Calculating curvature, however, requires more information. Equation 5 defines the geometric packing parameter, g ,²⁶ which consists of three components: (1) the individual surfactant volume, V_s , that is occupied by an average head and a tail, (2) the average head-silica interfacial area, a , and (3) the effective surfactant length, l , which is a sum of the effective tail length, l_c , and the head thickness, t_{head} . All parameters vary with temperature and are illustrated in Figure 5b and c.

$$g(T) = \frac{V_s(T)}{a(T)l(T)} \quad (5)$$

We know that the hydrothermal treatment of our composites drive changes in structure, surfactant curvature, and packing shape. Structures and possible corresponding packing shapes for various g values are listed in Table 5. The simplest way to visualize the surfactant shape change that corresponds to a hexagonal (cylinder phase)-to-lamellar (bilayer or interdigitated bilayer phase) transition is to consider a rearrangement from a truncated cone toward a cylinder. Such radially symmetric packing shapes do not easily assemble into cylinders, however, and so an equivalent way to visualize this same change in g -parameter is to imagine going from a pie wedge to a truncated pie wedge or rectangular solid, as illustrated in Figure 6a. While a cylinder has uniaxial symmetry, there is no reason to assume that each surfactant molecule in an anisotropic molecular environment must maintain cylindrical symmetry. In fact, imposing a cylindrical constraint on surfactants can lead to the conclusion that sphere-based phases should be stable for all surfactants with a g parameter less than 1—a conclusion that certainly is not born out by experiment.⁴² We thus believe that a pie wedge is the appropriate model for this system.

We expect both the surfactant volume, V_s , and the surfactant packing parameter, g , to increase with heating. Molecular thermal expansion simply dictates an increasing V_s . Furthermore, a surfactant tail expands faster than a surfactant head does, leading to larger g values and lower-curvature structures at higher temperatures. The presence of the silica framework, however, may lead to nonmonotonic behavior for either parameter, as suggested by the behavior of $a_0(T)$ in Figure 4.

C. Examining the Optimal Situation of Unconfined Surfactants. To determine how much the rigid

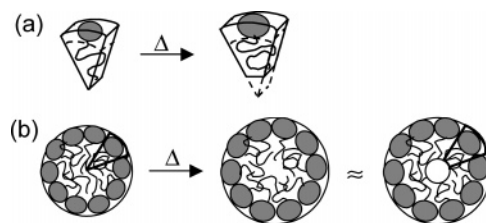


Figure 6. Hydrothermal treatment of composites drives surfactant packing changes. Specifically, the surfactant tail volume expands, but its radial length shrinks. The pie wedge (a) is used to depict such changes. Upon heating, it expands and becomes truncated. Because of this, heating a pore with uniform tail density may give rise to a low tail density center (b). This pore center can be modeled with an average zero tail density. This modeling captures basic aspects of surfactant packing in the composites and aids in understanding the hexagonal-to-lamellar phase transition.

silica framework frustrates surfactant packing, we must know the behavior of unconfined, unconstrained surfactants. Comparison of optimal surfactant behavior with a frustrated one should reveal whether volume effects or curvature effects, if either, provide the main drive for the observed structural changes. The optimal situation is described by the volume, V_{opt} , and the packing parameter, g_{opt} , that a surfactant prefers to possess. V_{opt} is simply the sum of surfactant tail and head volumes; according to eq 5, the packing parameter g_{opt} is made up of the optimal volume, V_{opt} , the optimal silica-surfactant interfacial area, a_{opt} , and the optimal radial surfactant length, l_{opt} .

We use Spartan molecular modeling software³⁷ to estimate the initial values for the volume, V_{head} , of the headgroup $\text{N}(\text{CH}_3)_3^+$ and for the head width, t_{head} , that is normal to the silica wall at room temperature. The thickness, t_{head} , is given as the electrostatic diameter of an unconfined $\text{BrN}(\text{CH}_3)_4$. Also, we estimate the initial optimal silica-surfactant interfacial area, a_{opt} , as the ratio of initial values for V_{head} and t_{head} . For the surfactant tail, the initial optimal volume, V_{tail} , is determined from the volumes of its molecular groups CH_3 and CH_2 ,⁴³ while the initial optimal length, l_c , is taken as the average length of several tails modeled through Spartan.³⁷ Table 6 provides all values discussed here.

The optimal volume evolves simply with the temperature-dependence of the different molecular volumes, as measured by Hagslätt and co-workers⁴³ and listed in Table 6. Equation 6 gives the final expression for V_{opt} . We note that each headgroup behaves independently of one another, whether belonging to a regular or gemini surfactant. Thus, the volume and thermal expansion coefficient of the average head in a gemini-containing composite include those values for one headgroup scaled by the appropriate gemini fraction x_{gemini} .

$$V_{\text{opt}}(T) = V_{\text{opt}}(T_{\text{initial}}) + \left[(1 + x_{\text{gemini}}) \frac{dV_{\text{head}}}{dT} + \frac{dV_{\text{tail}}}{dT} \right] (T - T_{\text{initial}}) \quad (6)$$

To examine the corresponding packing parameter, we must also know how the optimal interfacial area, a_{opt} , and optimal length, l_{opt} , change with heating. Changes in a_{opt} are calculated from T -dependent changes in the head volume (eq 7). Equation 8 supplies the length, l_{opt} , with the appropriate thermal expansion coefficient, which is simply the sum of the coefficients for t_{head} and l_c . Like a_{opt} , changes in t_{head} are calculated from the thermal expansion

(42) Tsonchev, S.; Schatz, G. C.; Ratner, M. A. *Nano Lett.* **2003**, *3*, 623.

(43) Hagslätt, H.; Söderman, O.; Jönsson, B. *Liq. Cryst.* **1992**, *12*, 667 and references therein.

Table 5. Geometric Packing Parameter, g , and Corresponding Geometries and Packing Shapes²⁶

g	aggregate structure	packing shape
$<1/3$	spheres	cone
$1/3-1/2$	cylinders	truncated cone or pie wedge
$1/2-1$	flexible bilayers or partially interdigitated bilayers	truncated cone or truncated pie wedge
~ 1	planar bilayers	cylinder or rectangular solid

Table 6. Calculated and Tabulated Geometric and Thermal Properties of Surfactants

group X	volume V_X (Å ³)	(dV_X/dT) (Å ³ /K)	t_{head} (Å)	l_c (Å)	((dl_c/dT)) _P (1/K)
tail: $-(\text{CH}_2)_{19}\text{CH}_3$	567.0 ^a	0.4569 ^a		20.5 ^d	-9.3×10^{-4} ^d
head: $-\text{N}(\text{CH}_3)_4^+$	118.03 ^c	0.05384 ^b	2.39 ^c		

^a From Hagsl  t et al.⁴³ Volumes are given at 273 K. ^b For $-\text{N}(\text{CH}_3)_3\text{Br}$ from Hagsl  t et al.⁴³ ^c From Spartan.³⁷ ^d From Kirk and Gr  ner data.⁴⁴ The l_c value, extrapolated from a linear fit to the data, is given for 0 K.

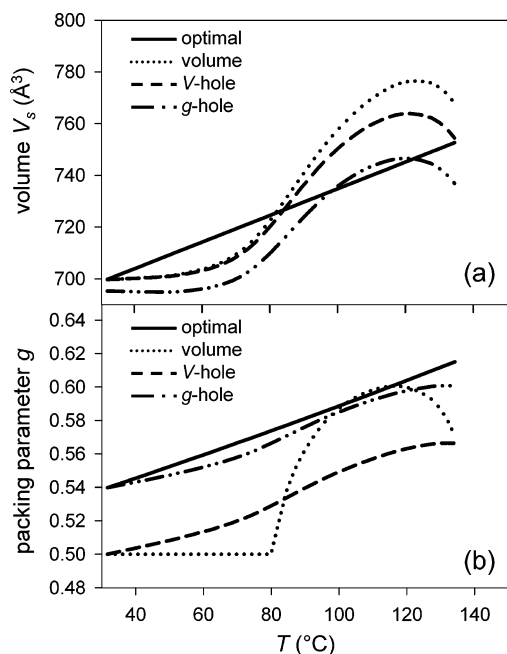


Figure 7. Available surfactant volume, V_s (a), and packing parameter, g (b), values for the 9.5% gemini sample. Solid lines represent the optimal situation; both V_s and g vary linearly with T . Other curves arise from different geometric models and illustrate deviations from optimal packing. In general, models reveal that excess pore volume but constrained curvature exist as the composite undergoes a hexagonal-to-lamellar transition.

of the head volume. The T -dependence for the tail length is determined by scaling expansion data collected by Kirk and Gr  ner⁴⁴ on similar surfactants. These data are scaled with our initial tail length, which varied slightly with our different models.

$$\frac{da}{dT} = \frac{2}{3} \frac{1}{t_{\text{head}}(T_{\text{initial}})} \frac{dV_{\text{head}}}{dT} \quad (7)$$

$$\frac{dl}{dT} = \frac{dt_{\text{head}}}{dT} + \frac{dl_c}{dT} = \frac{1}{3} \frac{1}{a_{\text{opt}}(T_{\text{initial}})} \frac{dV_{\text{head}}}{dT} + l_{c,\text{opt}}(T_{\text{initial}}) \left(\frac{dl_c}{dT} \right)_p \quad (8)$$

Figure 7a shows that V_{opt} increases linearly with temperature. Because a_{opt} and l_{opt} also have a linear dependence on T , g_{opt} must increase linearly with respect to temperature (Figure 7b).

D. Examining Surfactant Behavior in the Presence of Silica Walls. We have already alluded to the

restricting behavior imposed by the framework, forcing surfactant phase behavior to deviate from optimum. Certainly, surfactants may not completely fill or fit into this volume. Surfactants may not pack with their optimal shape and curvature either. As discussed earlier, we model our composites as hexagonally packed cylinders to capture this constraint and examine two different starting assumptions: (1) initial surfactant volume is optimized and (2) initial surfactant curvature is optimized. For each case, we calculate changes in the volume, ΔV_s , that is accessible to a surfactant and the corresponding packing parameter, Δg , with heating.

1. Calculations Based on Pore Volume and Optimized Surfactant Volume: The Volume Model. The simplest way to calculate volume and curvature changes for surfactants confined in hexagonally packed cylinders is to examine the case in which surfactant volume was optimized during synthesis. Thus, $V_s = V_{\text{opt}}$ at T_{initial} . In addition, the organic density is kept constant across the pores. Thus, the volume available to a surfactant is simply the formula for a solid cylinder, as given by eq 9 with pore diameter data for input. We note that knowing the number of surfactants, n_{surf} , and the total cylindrical length, h , explicitly is unnecessary since only the molecular volume is needed. We simply keep h/n_{surf} as a proportionality constant relating V_s to r_p and use eq 9 with the initial volume and pore radius values to calculate a constant h/n_{surf} . Finally, we apply eq 9 to propagate $V_s(T)$ with pore radii $r_p(T)$.

$$V_s(T) = \frac{\pi h}{n_{\text{surf}}} [r_p(T)]^2 \quad (9)$$

$V_s(T)$ values for this Volume model are given for the 9.5% gemini sample in Figure 7a and compared with $V_{\text{opt}}(T)$. Initial heating results in constrained surfactants; $V_s < V_{\text{opt}}$. The silica acts as a kinetic barrier that prevents surfactants from occupying their optimal volumes. Ultimately, with enough heating, the available pore volume exceeds the necessary surfactant volume; $V_s > V_{\text{opt}}$. Surfactants are no longer volume-frustrated, even for temperatures at which the hexagonal-lamellar phase transition begins. A simple expansive pressure supplied by the surfactant tails onto the silica framework thus does not appear to drive the phase transition.

Furthermore, similar behavior is found for all samples. We examine the volume expansion of our other composites with plots of $\Delta V_s(T) (=V_{\text{opt}}(T) - V_s(T))$ in Figure 8a. As each composite undergoes structural rearrangement, surfactants expand but do not need to access all available volume. Further heating, however, expands the organic phase faster than the ideal surfactant volume and ΔV_s rises at higher T for all composites. Except for the 16.2% gemini sample, the surfactant volume appears to become

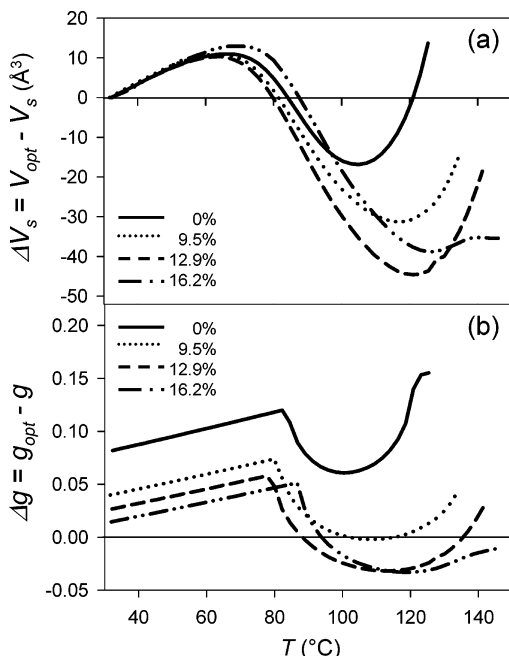


Figure 8. Differential changes of the available surfactant volume, V_s (a), and the packing parameter, g (b), for the Volume model. Volume expansion data reveals excess pore Volume as the composites transform. Curvature data, by contrast, reveal constrained packing shapes in some but not all cases. Surfactants show constrained curvatures with low gemini concentrations but unconstrained curvatures with high gemini concentrations. The latter result indicates that this model is too simple, as it provides no driving force for the phase transition with high gemini concentrations.

restricted again but only after the composite has begun transforming. Thus, at best, simple volume expansion *aids* the phase transition.

The packing parameter for a homogeneously filled right cylinder (and for this Volume model) has a constant value of 0.5. However, we know from XRD data that a phase transition occurs, and thus, g must change. To resolve this inconsistency, we impose that the organic density need not be constant across the pores. Because the available pore volume is found to be in excess at higher temperatures, we allow the surfactant to occupy its preferred volume when there is adequate space. In other words, the surfactant volume in eq 5 is the smaller of the available volume (eq 9) and the optimal volume (eq 6). When excess space exists, a hole at each pore center arises. Although such voids are unphysical, low-tail-density regions may be present. While the average surfactant tail length shrinks upon heating,⁴⁴ any tail in this fluid phase can occupy the entire radial length of its pore instantaneously. A small concentration of these extended tails at higher temperatures, therefore, gives rise to a low-density center. In Figure 6b, we illustrate these low-density centers as cylindrical voids. When a surfactant is able to occupy its desired volume, the volume of a surfactant within a pore is given by eq 10 with $V_s = V_{\text{opt}}$. Equation 10 can then be rewritten to solve for the tail length $l(T)$. Equation 11 provides a simple expression for a_s , the head-silica interfacial area in a cylindrical pore. Combining these expressions for $V_s(T)$, $l(T)$, and $a_s(T)$ into eq 5 leads to a variable volume-based packing parameter.

$$V_s(T) = \frac{\pi h}{n_{\text{surf}}} [(r_p(T))^2 (r_p(T) l(T))^2] \quad (10)$$

$$a_s(T) = \frac{2\pi h}{n_{\text{surf}}} r_p(T) \quad (11)$$

This model's $g(T)$ is plotted for the 9.5% gemini sample in Figure 7b with $g_{\text{opt}}(T)$. For about half the data, $g(T)$ is 0.5, which is consistent with surfactants occupying all available pore volumes and composites possessing a constant tail density across the pores. Also, for most temperatures, g is smaller than g_{opt} ; surfactants are constrained and unable to possess their desired curvature. As the temperature and the pore volume increase, this packing constraint relaxes slightly. The surfactants even reach their optimum shape (i.e., $g = g_{\text{opt}}$) briefly. However, Figure 8b reveals with plots of $\Delta g(T) = (g_{\text{opt}}(T) - g(T))$ that this behavior is not general for all four composites. At low and intermediate temperatures, Δg is positive for all composites and the framework prevents surfactants from packing into their preferred shape. At higher temperatures, however, only Δg for the 0% and 9.5% gemini samples remains positive. The remaining two samples, 12.9% and 16.2%, eventually produce negative Δg values, indicating that surfactant curvature is not constrained. Plots in Figure 8a, however, already indicate that, at the same time, extra pore volume exists. If neither the curvature nor the volume is constrained in the higher gemini fraction composites, there is no obvious reason for the continued structural change observed in these materials at temperatures above ~ 90 $^{\circ}\text{C}$. The emergence of negative values for both Δg and ΔV thus implies that our model is too simple and must be altered.

2. Calculations Based on Pore Volume and Realistic Surfactant Geometries: The V-Hole Model. Thus far, our simplest calculations reveal that neither limited volume nor constrained curvature consistently drive the phase transition observed as composites are subjected to hydrothermal treatment. Therefore, we further adjust our model and modify how low-density regions (or voids) evolve by putting molecular details into V_s and g . So far, atoms that make up the surfactants have sampled volume beyond what is acceptable; no molecular connectivity constraint has been imposed. Surfactants, however, are not infinitely flexible; their radial lengths are finite, and our volume and curvature calculations must account for this.

We include molecular connectivity by limiting the volume allowed to a surfactant. We accomplish this by forcing center voids to evolve with the average surfactant length, $l(T)$. Initially, this length is equal to the pore radius, but as the composite is heated, the tail shrinks.⁴⁴ Furthermore, the headgroup expands at a slower rate than the tail. Therefore, the overall surfactant length must decrease and the center void must grow. This length, $l(T)$, is determined by calculating its components, t_{head} and l_c . The head thickness, t_{head} , is solved by rearranging eq 12, which gives the cylindrical volume occupied by all heads. The head volume, $V_{\text{head}}(T)$, evolves optimally with values from Table 6, as described in section C. The tail length, $l_c(T)$, also evolves optimally but with a different initial value. This initial tail length is now the difference between the initial pore radius and the initial head thickness. Putting all these variables together, along with pore radii values, into eq 9 gives us $V_s(T)$ values for this V-hole model. Also, we now can determine the corresponding packing parameter, $g(T)$, by using eq 5 with the values of $V_s(T)$ and $l(T)$ for this model. The interfacial area, $a_s(T)$, is described

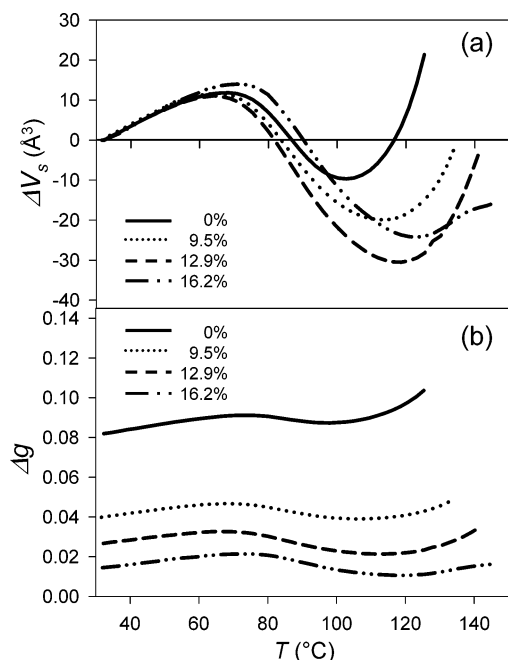


Figure 9. Differential changes of the available surfactant volume, V_s (a), and packing parameter, g (b), when the volume is initially optimized (V-hole model). Generally, at the onset of the phase transition, adequate volume is available but curvature is frustrated. Positive Δg values for all temperatures suggest that the phase transition is mainly curvature-driven.

again by eq 11, which was established in the previous model.

$$(1 + x_{\text{gemini}})V_{\text{head}}(T) = \frac{\pi h}{n_{\text{surf}}}[(r_p(T))^2 - (r_p(T) - t_{\text{head}}(T))^2] \quad (12)$$

$V_s(T)$ data for the 9.5% gemini sample for this V-hole model are plotted in Figure 7a. Corresponding $\Delta V_s(T)$ values for our four composites are given in Figure 9a. Trends observed here are similar to those observed in the previous simpler model. Initial heating causes ΔV_s to become positive; surfactants are constrained. At intermediate and higher temperatures, ΔV_s becomes negative and excess pore volume arises. Eventually, for all but the 16.2% gemini sample, ΔV_s becomes positive again. Even so, this constrained situation occurs *after* the initial stages of the phase transition. Like the previous model, our V-hole model indicates that simple volume expansion may help but does not drive structural change.

To see if curvature effects drive the phase transition, we examine the corresponding packing parameter plotted for the 9.5% gemini sample in Figure 7b. Unlike the packing parameter in the previous model, this g is greater than g_{opt} for all temperatures; surfactants are always constrained and unable to possess optimal curvature. In Figure 9b, Δg plots for this V-hole model reveal that all four samples exhibit the same behavior and that surfactants are constrained throughout the heating process. However, Δg decreases as ΔV_s decreases or as the gemini surfactant concentration increases. Some of the constrained packing is alleviated by excess available volume, whether the excess pore volume arises from pore expansion or from a lower tail density. The latter trend supports the results presented in Figure 3b; decreasing tail density should produce a less-frustrated curvature, which should yield a higher $T_{\text{transition}}$. Still, overall curvature remains frustrated at all temperatures. These packing effects

appear to propel the phase transition, and composites now have a driving force for structural change. We note that, although Δg values are small in magnitude, they are not negligible.

3. Calculations Based on Realistic Surfactant Models but with Packing Optimized during Synthesis: The g-Hole Model. In the previous sections, we initially assumed that surfactant volume was optimized. Ideally, as-synthesized composites contain unfrustrated surfactants that also occupy desired packing shapes. The silica simply provides a framework around the cylindrical micelles. However, composite structures are unlikely to have surfactants that possess *both* ideal volumes *and* ideal curvatures. Therefore, in this section, we examine a final limiting situation—we impose the constraint that curvature is optimized, rather than volume, during synthesis. Reality likely lies somewhere between these two limiting assumptions.

If surfactants initially pack with optimum curvature, low-tail-density regions must reside at the pore centers from the start. By approximating such regions again as voids, we can use eq 10 to calculate the pore volume available to a surfactant with pore radii and surfactant lengths as input. The length, $l(T)$, is computed in the same fashion as in the previous V-hole model but with a different initial value.

$$l(T_{\text{initial}}) = 2r_p(T_{\text{initial}})[1 - g_{\text{opt}}(T_{\text{initial}})] \quad (13)$$

The initial value for l is determined by imposing our assumption that curvature is optimized initially into eq 5. We rewrite this g expression in terms of $r_p(T_{\text{initial}})$ and $l(T_{\text{initial}})$ by replacing V_s and a_s with their expressions in eqs 10 and 11. The length $l(T_{\text{initial}})$ is then isolated, leading to the final expression in eq 13. We also can now calculate $V_s(T_{\text{initial}})$. Initial pore radii values for our composites are listed in Table 4. The packing parameter for this g-hole model is again calculated with eq 5 using the surfactant volumes $V_s(T)$ and lengths $l(T)$ described above. Equation 11 gives values for the interfacial area, $a_s(T)$.

The g-hole model $V_s(T)$ plot for the 9.5% sample is added to Figure 7a and exhibits behavior similar to the available pore volumes from other models. V_s increases with temperature but then decreases as composites prepare to transform. Initially, V_s is less than V_{opt} , but around 100 °C, V_s becomes slightly greater than V_{opt} . Surfactants are no longer constrained and can fill their desired volumes. Further heating leads V_s to become smaller than V_{opt} , and above 120 °C, surfactants are constrained once more. In addition, unlike the V-hole model, the start of the phase transition does not precede but rather coincides with surfactant volume becoming frustrated again. We examine the other samples and present plots of the corresponding ΔV_s values in Figure 10a. $\Delta V_s(T)$ for the 12.9% gemini sample behaves similarly to that for the 9.5% gemini sample and regains a positive ΔV_s soon after the phase transition has begun. Although ΔV_s data for the 16.2% gemini sample remains negative to the end, ΔV_s approaches positive values at the highest temperatures. In contrast, $\Delta V_s(T)$ values for the 0% gemini sample are positive for *all* temperatures, indicating that surfactant volumes are always volume-frustrated when no gemini surfactants are present. Because of this inconsistent picture painted across gemini concentrations, it does not appear that volume-constrained surfactants provide the main driving force for structural change.

If a frustrated volume does not drive the phase transition in this model, perhaps a frustrated curvature does. Figure 7b reveals that the relevant packing parameter is slightly smaller than g_{opt} for all temperatures for the 9.5% gemini

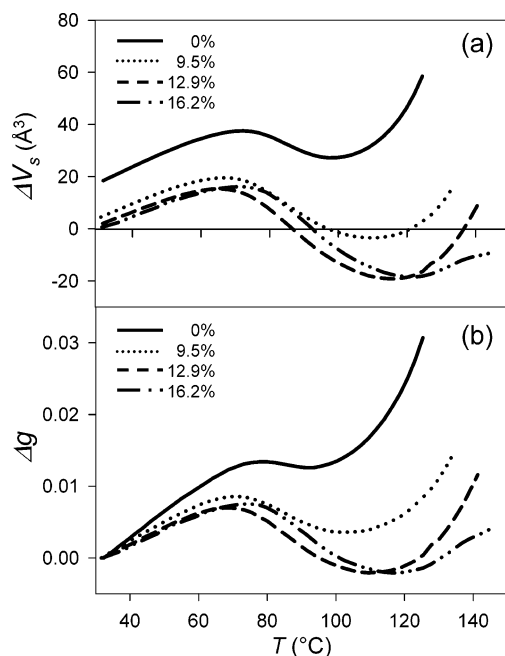


Figure 10. Differential changes of the available surfactant volume, V_s (a), and packing parameter, g (b), when curvature is initially optimized (g -hole model). Like the V -hole model, excess volume is available but curvature is frustrated as composites transform. Positive Δg values prior to the onset of structural changes suggest a predominantly curvature-driven phase transition.

sample. Although this model optimizes shape initially, surfactant curvature quickly becomes and remains frustrated throughout the entire heating process. This behavior is general for our four composites, as illustrated in Figure 10b plots of $\Delta g(T)$. However, interesting behavior occurs for the 12.9% and 16.2% gemini samples around 110–115 °C; curvature appears to be briefly optimized, and within our significant figures, g is equal to g_{opt} . These results may be an artifact of our model as XRD data reveal no plateau of a_o values. The more-significant result is that with further heating the surfactant curvature again becomes constrained before the phase transition and the value of Δg increases rapidly at these higher temperatures. Thus, frustrated curvature is present prior to the onset of the phase transition, and the degree of frustration increases rapidly for any remaining hexagonal material; as the temperature increases, the transition progresses. This curvature frustration most likely provides the dominant driving force for restructuring.

E. Additional Restructuring: Annealing. So far, we have examined the role played by surfactant packing as these silica/surfactant composites undergo major restructuring that results in a phase transformation. The data in Figures 2 and 4, however, suggest that significant structural change takes place while the composite is in the hexagonal structure. This subtle restructuring has been dubbed annealing and has been the focus of a number of previous studies.^{45–49} Annealing describes the heating process that leads to a more-homogeneous hexagonal

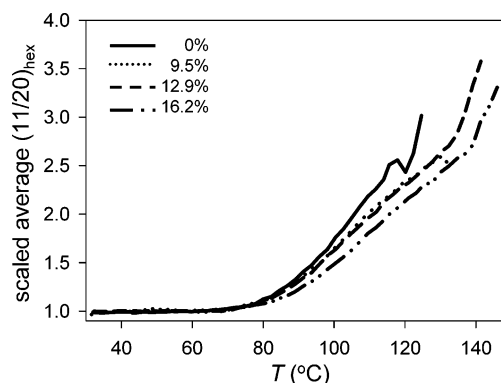


Figure 11. Prior to transformation, the silica framework anneals toward a more-uniform hexagonal structure. Annealing is tracked through the ratio of higher-order (11)_{hex} and (20)_{hex} peak areas and begins around 80 °C in all cases. The data show that the structural changes proceed more rapidly with heating for the 0% gemini sample than for the 16.2% gemini sample. Moreover, the onset of annealing coincides well with the onset of frustrated surfactant packing (see Figures 8–10). The results suggest that this restructuring of the hexagonal phase is also a curvature-driven process.

structure.⁴⁶ Low-density regions or small voids in the silica wall that form during the self-assembly process condense, producing a more-uniform wall structure.^{45–49}

Annealing is tracked by plotting the evolution of the (11):(20) hexagonal peak area ratio with heating; the (11)_{hex} peak area increases relative to the (20)_{hex} peak area as the composites are heated (Figure 2).⁴⁶ Plots of this ratio as a function of temperature are shown in Figure 11 for our four composites. For proper comparison, we scale the four curves by their initial average (11):(20) ratio, which is the average of the ratios at lower temperatures in the plateau region of the curve. Annealing begins when this scaled (11):(20) ratio begins to rise. This annealing onset has been assigned to tail melting in the surfactant⁵⁰ and thus to the point where the tail volume begins to increase significantly. As seen in Figure 11, this annealing onset is very similar for all the samples, suggesting that the initial tail density is, in fact, nearly the same for all samples. Figure 11 does show, however, that the rate of increase of the (11):(20) peak area ratios clearly depends on the gemini content with samples that contain a larger fraction of gemini surfactant showing the least change with increasing temperature.

Comparing the result in Figure 11 with the corresponding plots in Figures 8a and 9a reveals that ΔV_s for the Volume model and the V -hole model, respectively, is negative when annealing begins. Surfactant volume is not apparently constrained as the hexagonal periodicity begins to improve. For the g -hole-model ΔV_s in Figure 10a, three of the four gemini samples also exhibit the same behavior. That is, although slightly constrained when annealing begins, volume does not remain frustrated as annealing continues. Thus, volume-frustrated surfactants do not appear to drive annealing.

Comparing the Δg plots in Figures 9b and 10b with the annealing curves in Figure 11, on the other hand, reveal that the onset of curvature frustration in these surfactants coincides well with the start of annealing. (We ignore Figure 8b plots at this time since these Δg values arise from less-realistic modeling.) Furthermore, the specific Δg values agree with the annealing trends as a function of gemini concentration. Curvature is most constrained

(45) Impérator-Clerc, M.; Davidson, P.; Davidson, A. *J. Am. Chem. Soc.* **2000**, *122*, 11925.

(46) Lindén, M.; Blanchard, J.; Schacht, S.; Schunk, S. A.; Schüth, F. *Chem. Mater.* **1999**, *11*, 3002.

(47) Schacht, S.; Janicke, M.; Schüth, F. *Micropor. Mesopor. Mater.* **1998**, *22*, 485.

(48) Edler, K. J.; Reynolds, P. A.; White, J. W.; Cookson, D. *J. Chem. Soc., Faraday Trans.* **1997**, *93*, 199.

(49) Gross, A. F.; Le, V. H.; Kirsch, B. L.; Riley, A. E.; Tolbert, S. H. *Chem. Mater.* **2001**, *13*, 3571 and references therein.

(50) Gross, A. F.; Yang, S.; Navrotsky, A.; Tolbert, S. H. *J. Phys. Chem. B* **2003**, *107*, 2709.

for the 0% gemini sample for which annealing occurs at a slightly faster rate. For the 16.2% gemini sample, on the other hand, curvature is least constrained and annealing occurs at a slower rate. Therefore, in addition to driving mesostructural phase changes, curvature frustration in these surfactants appears also to help drive other types of nanoscale restructuring, even if such frustration does not result in a change of symmetry of the composite material.

Conclusions

This work emphasizes the importance of the surfactants as structural-directing agents and shows the hexagonal-to-lamellar phase transition is a surfactant-curvature-driven process. We find that increasing gemini concentration and thus lowering the tail density within the pores raises the hexagonal-to-lamellar phase transition temperature. This trend supports the idea that heating causes surfactant tails to be more mobile. Such thermal disorder contributes significantly to changes in surfactant curvature and packing shapes. A composite with a lower tail density, therefore, requires more thermal energy for its surfactants to expand to the necessary packing shapes needed to drive the phase transition.

Various geometric models are used to calculate volume and curvature changes. Because of the observed liquid-crystal-like behavior, we quantify curvature with Israelachvili's packing parameter, g .²⁶ Although none of the simple limiting models presented here are a perfect representation of the actual volume and curvature changes that occur upon heating a silica/surfactant composite under hydrothermal conditions, they all provide a remarkably consistent picture of the basic behavior. The composites form in such a way that the volume and the curvature of the surfactant are nearly optimized. During synthesis, however, a rigid silica framework is formed, so the composite structure becomes locked in this geometry. Upon heating, the surfactant tails become fluid and increase in volume. This causes both an expansion of the overall pore diameter and a loss of any low density regions in the wall (a process that we call annealing). While both pore expansion and annealing can increase the available pore volume, they cannot produce a curvature that is optimal for surfactant packing, and so with sufficient heating, a phase transition from a higher-curvature hexagonal phase to a lower-curvature lamellar phase

occurs. Together, the three models thus establish that, while volume-frustrated surfactants can help drive structural change, rearrangement of the silica framework is mainly curvature driven. This work nicely corroborates previous work of Gross and co-workers,²³ which used the observation of an intermediate phase to conclude that the hexagonal-lamellar phase transition is a curvature-driven process.

Our numerical results for volume and curvature evolution provide strong evidence that curvature-frustrated surfactants drive the hexagonal-lamellar phase transition. We confirm that Israelachvili's geometric packing parameter, g ,²⁶ can be applied when examining the surfactant phase behavior of our composites. Therefore, although the presence of the highly cross-linked inorganic framework may hinder a phase change, surfactant packing continues to play a major role in determining final structures. Our results also establish that small adjustments to the head:tail density ratio are a straightforward way to alter g slightly without disrupting the overall mesostructure. Tailoring surfactant curvature allows the composite's phase behavior and hydrothermal stability to be modified. Composites are most stable when surfactant curvature matches pore curvature.⁵¹ Therefore, a high-curvature composite produced with surfactants of slightly lower average curvature alleviates some of the added packing constraints as samples are subjected to hydrothermal treatment, a process which is commonly used to produce more-condensed, more-robust materials.

Acknowledgment. We gratefully acknowledge the assistance from M. J. Strouse with NMR spectroscopy, from J. Wu with XRD and N₂ adsorption/desorption studies, and from V. H. Le with composite synthesis. A.M.L. acknowledges the support of a UC Regents Dissertation Fellowship. This manuscript includes data collected at the Stanford Synchrotron Radiation Laboratory, which is operated by the Department of Energy, Office of Basic Energy Sciences. This work was supported by the National Science Foundation under Grant Nos. DMR-9807190 and CMS-0307322 and by the Beckman Young Investigator Program. S.H.T. is an Alfred P. Sloan Foundation Research Fellow.

LA048505G

(51) Xia, Y.; Mokaya, R. *J. Mater. Chem.* **2003**, *13*, 3112.